Nuclear Materials and Energy 39 (2024) 101661

Contents lists available at ScienceDirect

Nuclear Materials and Energy

journal homepage: www.elsevier.com/locate/nme

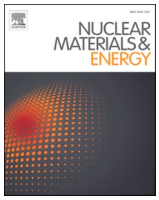

A novel solution for hydrogen monitoring in fusion processes: 3D printed $BaCe_{0.6}Zr_{0.3}Y_{0.1}O_{3-\alpha}$ sensors

Antonio Hinojo, Enric Lujan, Jordi Abella, Sergi Colominas *

Electrochemical Methods Laboratory – Analytical and Applied Chemistry Department, IQS School of Engineering, Universitat Ramon Llull, Via Augusta 390, 08017 Barcelona, Spain

ARTICLE INFO

Keywords:
Stereolithography
Amperometric
Potentiometric
Hydrogen sensor
BCZY
Electrochemical monitoring

ABSTRACT

The control of tritium (^3H) in liquid-based tritium breeding blankets (TBBs) is one of the key points to assure their correct performance to prove the ^3H sufficiency. For that, electrochemical sensors are a good option for tritium quantification since they can perform in-situ and online measurements.

One of the multiple challenges for hydrogen detection is to find suitable materials that can operate at high temperatures and in harsh environments. In this context, perovskite-type ceramics, such as $BaCe_{0.6}Zr_{0.3}Y_{0.1}O_{3-\alpha}$ (BCZY), have elevated proton conductivity and exceptional stability even in reducing atmospheres and at elevated temperatures, which make them strong contenders for high-temperature hydrogen sensing applications.

In the present study, we describe the development of a dual-mode hydrogen sensors based on 3D-printed BCZY, which allows a high degree of design flexibility. Crucible geometries were tested and characterized using X-ray diffraction and scanning electron microscopy. Electrochemical sensors were constructed and characterized at 400, 450 and 500 °C in both, amperometric and potentiometric configuration. The results demonstrated the capability of 3D-printed BCZY sensors for hydrogen detection in fusion reactors, offering a breakthrough solution for monitoring fusion processes.

1. Introduction

The progress in the search for cleaner and more efficient energy sources has led to a growing interest in nuclear fusion as a promising alternative. However, the precise and reliable measurement of hydrogen isotopes at high temperatures is one of the challenges in the practical realization of this process. Traditional offline analytical methods cannot measure the dynamic changes that occur during high-temperature hydrogen processes. As a result, in-situ measurement tools capable of real-time monitoring are clearly needed. Within this context, electrochemical devices are a great option because of its low power requirements, excellent repeatability and accuracy [1], also in fusion applications.

For high temperature applications, electrochemical sensors can use both molten salts like $CaCl_2 + CaH_2$, as proposed by Holstein et al. [2–4], or proton-conducting solids as electrolytes. In the latter case, perovskite-structured oxides are great candidates since they present proton conduction typically from 300 to 1000 °C [5]. Perovskite oxides are characterized by their ABO_3 composition, where A is typically occupied by large cations and B by transition metals. This structure creates an octahedral assembly of corner-sharing oxygen atoms surrounding the B-site cations. This structural arrangement in oxide perovskites is crucial for understanding the Grotthuss ionic conduction mechanism [6]. The mobility of ions in these structures is caused by oxygen vacancies and the mobility of ions in the octahedral sites. At high temperatures, thermal energy provides sufficient activation for protons to overcome energy barriers and jump from one oxygen site to another [7,8]. The oxygen atoms act as proton acceptors and donors, enabling the transfer of protons through the material using hydrogen bonds. Hydrogen bonds can be easily broken and reformed, allowing for the rapid transfer of protons. As a result, protons can move through the perovskite-structure oxide, facilitating ionic conductivity [9].

The use of these proton-conductor materials as solid-state electrolytes allows the sensors to work in the two most common modes of operation: amperometric, which measure current, and potentiometric, which measure potential difference. Amperometric sensors typically are more adequate for the determination of low hydrogen concentrations of the analyte with high sensitivity, while potentiometric sensors are better to determine high concentrations [10].

Conventionally, uniaxial pressure is the technique used to shape this

* Corresponding author.
E-mail address: sergi.colominas@iqs.url.edu (S. Colominas).

https://doi.org/10.1016/j.nme.2024.101661
Received 20 October 2023; Received in revised form 16 April 2024; Accepted 23 April 2024
Available online 24 April 2024

type of materials [11,12]. This method is easy and inexpensive; however, it is limited to the production of disk-shaped specimens with a fixed geometry. This shape difficult the sealing process of the electrolyte in the sensor's structure for the industrialization of the process [13]. To address this challenge, alternative shaping techniques like ceramic mold casting [13], cold isostatic pressure (CIP) [14] or 3D printing [15] can be employed. It is worth mentioning that, slip casting may present cracks during the pouring process or when removing the sample from the mold, whereas cold isostatic pressure typically involves CNC (Computer Numerical Control) machining of the green body. In contrast, 3D printing technologies, such as stereolithography, offer a more convenient alternative with fewer drawbacks compared to traditional methods.

In the present work, dual-mode electrochemical sensors able to measure in both, amperometric and potentiometric mode, were developed and tested. For that, one-end closed tubes of $BaCe_{0.6}Zr_{0.3}Y_{0.1}O_{3-\alpha}$ proton-conductor perovskite material were 3D-printed using stereolithography. This ceramic was selected according to previous works [15–17]. Then, the samples were characterized after a debinding and sintering process using X-ray diffraction (XRD) to determine the crystal structure and a scanning electron microscope (SEM) to evaluate the layers adhesion and the sintering quality. Finally, electrochemical sensors were characterized at different hydrogen partial pressures at 400 °C, 450 °C and 500 °C. The sensitivity, response and recovery time, precision, and accuracy were evaluated in both configurations.

2. Materials and methods

2.1. $BaCe_{0.6}Zr_{0.3}Y_{0.1}O_{3-\alpha}$ shaping and characterization

The proton conductor material used as electrolyte, $BaCe_{0.6}Zr_{0.3}Y_{0.1}O_{3-\alpha}$ (ID code: BCZY), was prepared as described in previous works [16]. Then, crucibles were obtained (OD: 13 mm, ID: 11 mm, Length: 50 mm) using a stereolithography 3D printer. The slurry preparation and the printing process were performed by Lithoz Gmbh in Vienna. A debinding thermal program was performed to the green body at 450 °C for 86 h. Then, a sintering thermal program was applied at a rate of 5 °C·min^{-1} until 1700 °C – 2 h, followed by 1650 °C – 12 h.

The Archimedes principle was used to determine the bulk density of the crucibles. Samples were also analysed using X-Ray diffraction (XRD, Malvern Panalytical Empyrean, Cu Kα radiation). A Jeol JSM-5310 scanning electron microscopy (SEM) was employed to determine the 3D printing and the sintering quality.

2.2. Sensor construction

Sensors were constructed as depicted in Fig. 1.

As shown in Fig. 1, the 3D-printed BCZY crucibles (1) were coated with Pt to act as electrodes (2). Then, the platinized samples were cured at 1000 °C – 1 h. The crucibles were bound to an alumina tube (3) (Ø15 mm, 2 mm thickness, Length: 200 mm) using a glass cement (4). The sealant was cured at 900 °C – 30 min. The heating and cooling were controlled (150 °C·h^{-1}) to prevent cracks in the sealant. Then, the platinum electrodes were connected to a potentiostat using platinum wires (5). The constructed sensor can work both, amperometric and potentiometric mode. The external face of the platinized crucible was the working electrode (WE) and the inner face was the reference (RE) or the counter (CE) electrodes. The RE/CE electrode gas was introduced in the interior of the sensor using an alumina tube (6). This RE/CE gas inlet tube and the RE/CE platinum wire were inserted through a stainless-steel feedthrough (7) to electrically insulate the RE/CE electrode from the surroundings.

2.3. Electrochemical measurements

Sensors were tested inside a reactor (see Fig. 2) made of stainless-steel. Temperature was PID-controlled using a 1.5 kW heating element and a K-type thermocouple.

As shown in Fig. 2, the extreme of the thermocouple was placed near the sensor. This temperature was considered as the WE temperature. The system was finally covered with glass wool to assure a stable temperature.

Measurements were performed at 400, 450 and 500 °C using a Metrohm Autolab PGSTAT204 potentiostat. The hydrogen mixtures used for the experiments were obtained by mixing a 1000 ppm (1 mbar) H_2 in Ar calibration mixture with argon (quality 5.2). The gases supplier was Carburos Metálicos. Gas mixtures were done with Bronkhorst EL-FLOW flow controllers.

When the sensors worked in potentiometric configuration, it operated like a concentration cell. In this case, the WE hydrogen concentration ranged between 0.020 and 1.000 mbar H_2 in argon. A calibration

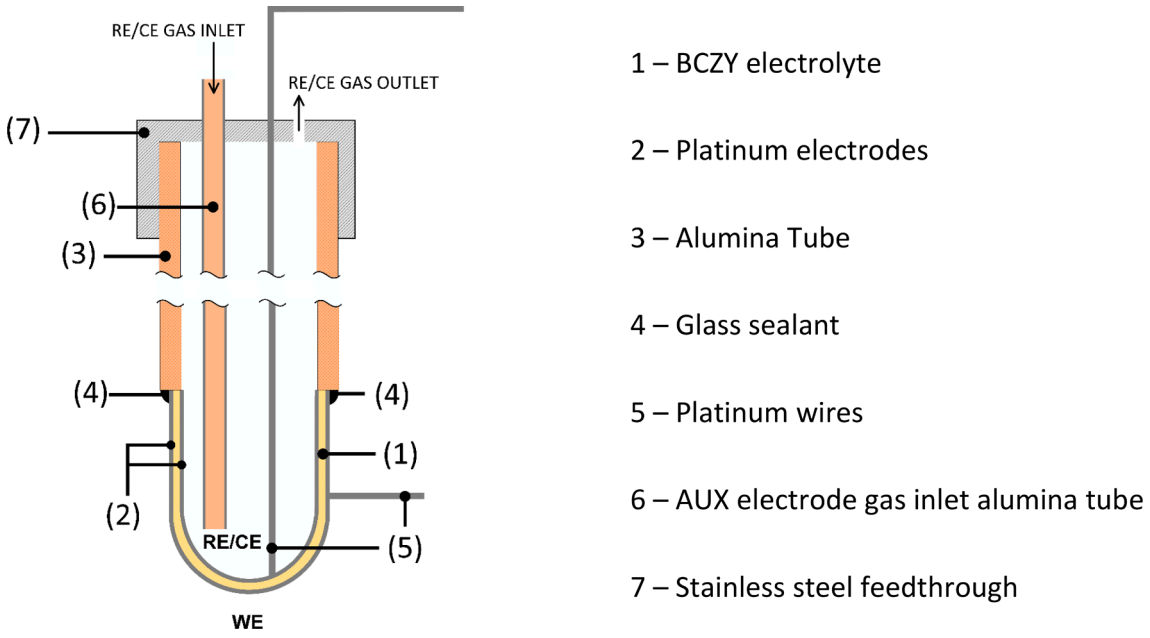

Fig. 1. Scheme of the constructed sensors. (WE: Working electrode; RE: Reference electrode (potentiometric mode), CE: Counter-electrode (amperometric mode)).

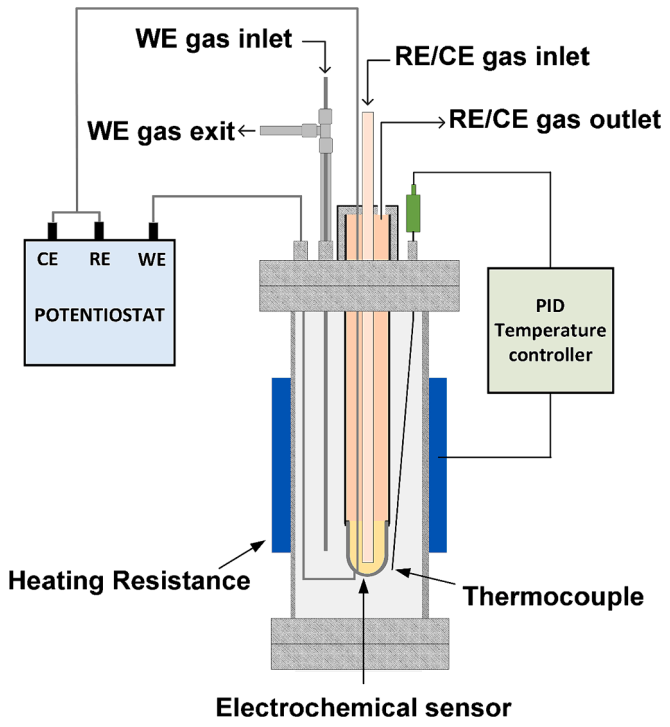

Fig. 2. Scheme of the reactor used for the electrochemical measurements.

mixture of 1.000 mbar of H_2 in Ar was used in the RE. The different H_2 partial pressure in the electrodes caused a potential difference, which is described with the Nernst equation:

$$\Delta E = \frac{RT}{2F} \cdot \ln\left(\frac{P_{H_2\,RE}}{P_{H_2\,WE}}\right) \quad (1)$$

In contrast, in the amperometric mode, the WE H_2 partial pressure ranged between argon and 0.040 mbar H_2. In this case, when a potential difference is applied between electrodes, the following electrochemical reaction happens in the WE:

$$H_{2(g)} \rightarrow 2H^+ + 2e^- \quad (2)$$

Thus, protons generated can move through the BCZY electrolyte from the WE to the CE. In order to evacuate the hydrogen generated in the CE, an argon flow is used as purging gas in this electrode. Therefore, a calibration curve can be obtained between the corrected intensity and the P_{H2}. The intensity was corrected by subtracting the signal obtained with pure argon to all the current measurements.

3. Results and discussion

3.1. Crucibles characterization

3D-printed specimens were sintered in air at 1700 °C for 2 h, followed by 1650 °C for 12 h. In previous works, specimens obtained with extrusion-based 3D printing needed a sintering process at 1700 °C − 1 h [31]. Nevertheless, the specimens obtained in this work presented more organic binders, which needed a longer sintering process to achieve high densification. Crucibles' bulk density was determined after the sintering thermal process in order to evaluate the densification of the pieces. The measured density was (6.09 ± 0.05) g·cm^{-3}, which corresponded to a densification of (97.9 ± 1.0) % compared to the theoretical density [18]. This value was high-enough in order to assure a gas-tight solid-state electrolyte [19]. Fig. 3A and B show the surface and cross-section of the crucibles by SEM after sintering.

As can be observed in Fig. 3-A, a dense surface could be observed. No imperfections or cracks could be appreciated. In Fig. 3-B it is shown that the printing layers could not be appreciated in the cross-section image. This fact indicated good adhesion between the layers that composed the crucibles. In addition, no channels that could negatively impact in the gas-tightness could be appreciated.

Crystal structure of the crucibles was also evaluated using X-ray diffraction (see Fig. 4).

The XRD pattern (Fig. 4) shows that sintered samples presented a cubic perovskite phase (ICDD # 04-017-6645, Pm-3 m). However, it can also be observed few small peaks that, after a phase identification, were associated to $Ba_5(OH)(PO_4)_3$ (ICDD # 01-078-1141, space group P63/m). This product was generated during the debinding and sintering process as an undesired reaction between the compounds used in the slurry preparation for 3D-printing and the barium present in the BCZY ceramic. In order to quantify these phases, the pattern was Rietveld refined. The quantities were 92.4 % for BCZY and 7.6 % for $Ba_5(OH)(PO_4)_3$. Although this last value seems significant, the actual effect will be addressed in the electrochemical results sections. Finally, the lattice

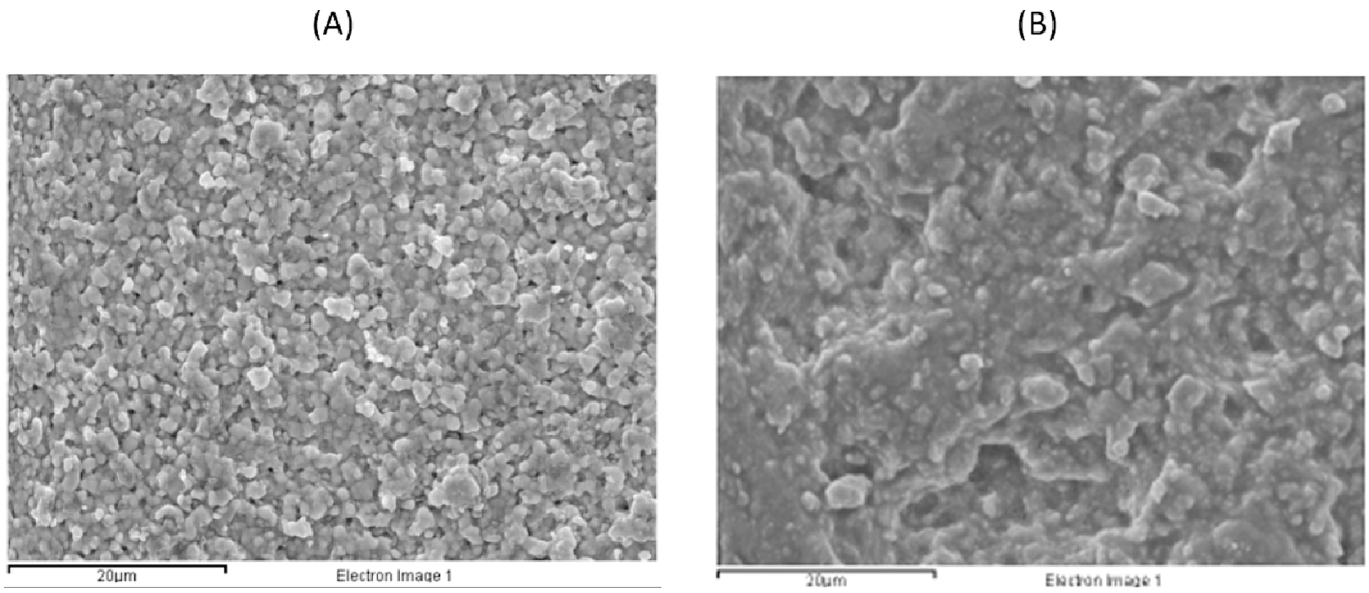

Fig. 3. Micrographs of 3D printed crucibles after the sintering thermal process: (A) surface and (B) cross-section.

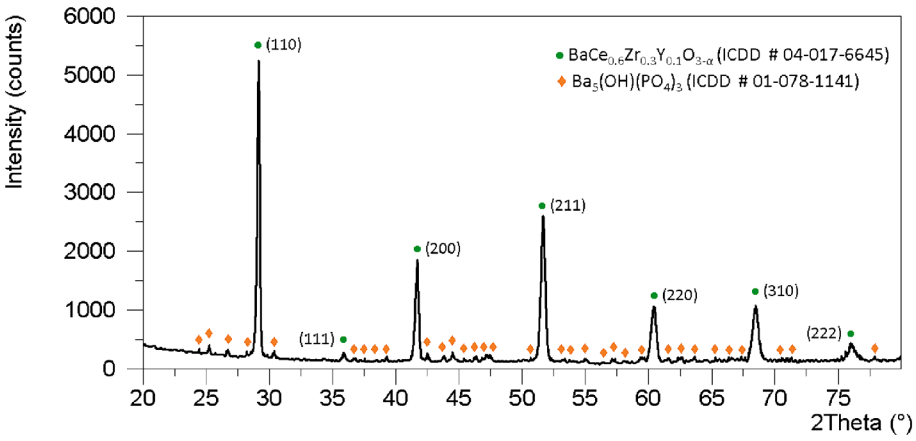

Fig. 4. X-ray diffractogram of 3D-printed crucibles after the sintering thermal process.

parameter obtained after the Rietveld refinement was 4.3310 Å. The theoretical value was 4.3300 Å. Therefore, the discrepancy between the experimental and the theoretical lattice parameter was 0.02 %, which indicates that there was no significant barium volatilization [20] and the presence of the abnormal phase did not significantly disturb the cubic structure of BCZY.

3.2. Potentiometric mode

3.2.1. Sensors' calibration

Once the sensors were constructed, they were evaluated in potentiometric configuration at 400, 450 and 500 °C. Measurements were performed between 0.020 and 1.000 mbar of H_2 in Ar using three different sensors. As example, Fig. 5 shows the ΔE – time plot at different H_2 partial pressures at 400 °C.

Fig. 5 shows quick variations in the ΔE after changing the H_2 partial pressure. As described by the Nernst equation, the potential decreased when the concentration in the WE increased. It can also be observed low oscillation (<1 mV) in the ΔE after the stabilization of the signal. Calibration plots were obtained by plotting the stabilized potential at each partial pressure in front of the $\ln(P_{H2,WE})$.

Fig. 6 depicts the calibration curves obtained at 400, 450 and 500 °C. Curves predicted with the Nernst equation are also represented. The standard deviation between measurements was indicated with error bars.

Fig. 6 shows that a linear trend was obtained at the three temperatures evaluated. At 400 °C, the linear range was observed between 0.020 and 0.500 mbar. At 450 °C and 500 °C, the linear range was widened to 0.020 – 1.000 mbar. In all the cases, it could be observed low deviations with respect the Nernst equation (dotted line). The sensors showed great reproducibility, as indicated by the small error bars in Fig. 6. Table 1 shows the calibration curves data obtained at each temperature.

Table 1 shows a linear trend between the ΔE and the $\ln(P_{H2})$, since the R^2 were higher than 0.99 [21]. Moreover, when the slopes and the Y-intercepts were compared with the theoretical ones (Nernst equation), in all cases low deviations were obtained. The maximum deviation in the slope was –3.9 % at 500 °C, while the maximum deviation in the Y-intercept was –6.1 % at 400 °C. All the deviations were lower than 10 %. Thus, the sensors showed a nernstian behavior. Limit of detection (LOD) was also calculated, according to [22], and it was 0.008 mbar at the three temperatures.

3.2.2. Dynamic response-recovery curve

Response and recovery time was also measured after the determination of the nernstian behavior. For that, a dynamic response and recovery curve (DRR curve) was performed. The initial H_2 concentration was stablished at 0.020 mbar. This value was considered as the recovery concentration since it is the lowest concentration within the calibration curve. Then, hydrogen concentration was increased randomly between 0.030 and 1.000 mbar of H_2 in Ar. After the stabilization of the potential difference of each concentration, the initial partial pressure was recovered (0.020 mbar). Response and recovery times were calculated as the period needed to achieve a 90 % of the steady potential [23]. As an example, Fig. 7 shows a DRR curve obtained at 400 °C.

Fig. 7 shows a quick detection of hydrogen partial pressure changes. Moreover, the initial concentration (0.020 mbar) was recovered in all

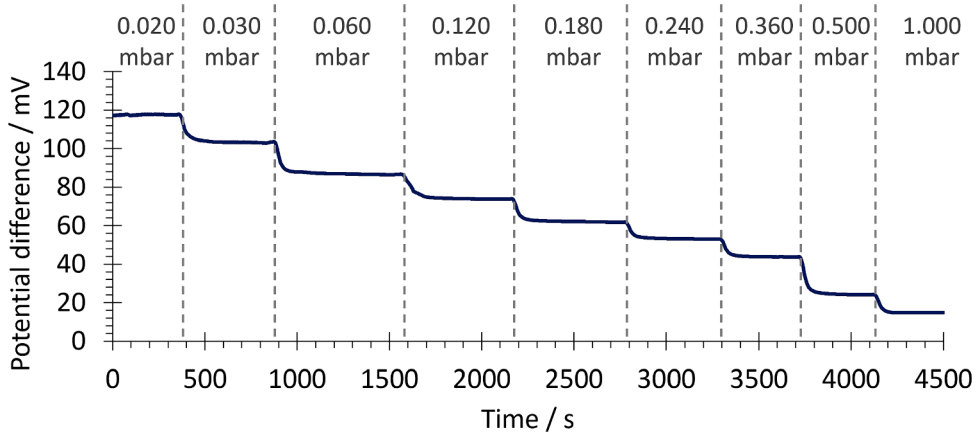

Fig. 5. Potential difference vs. time at each H_2 partial pressures obtained with the electrochemical sensor working in potentiometric configuration at 400 °C.

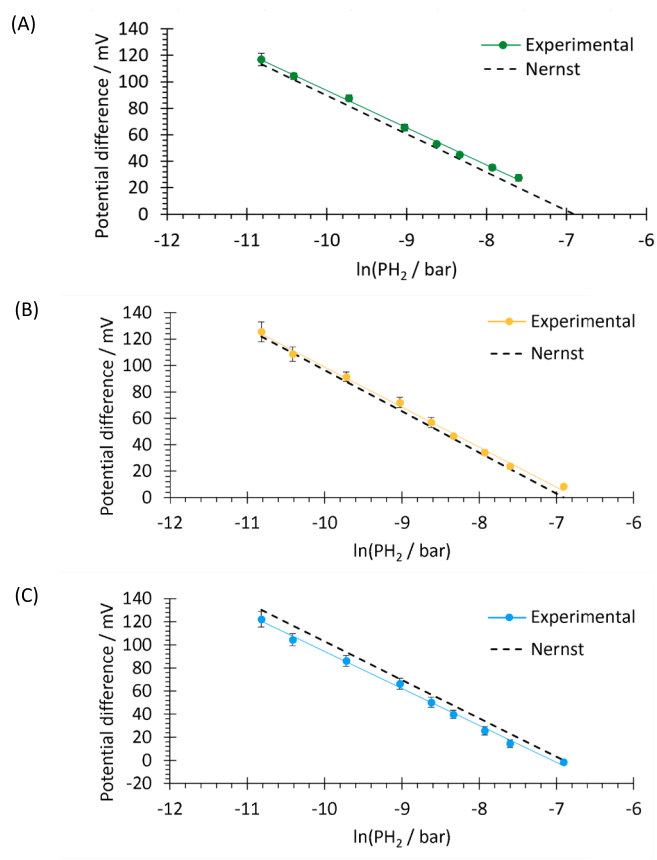

Fig. 6. Calibration curves obtained at (A) 400 °C, (B) 450 °C and (C) 500 °C.

the cases, i.e. no memory effect is detected. The potential differences registered at all the partial pressures were similar to those used in the calibration curves. Therefore, with the curves obtained at each temperature, the response and recovery times were plotted in Fig. 8.

As it is shown in Fig. 8, the response time was similar at 400 °C and 450 °C (55 s and 47 s, respectively) and slightly higher at 500 °C (76 s). In terms of recovery time, it can be observed that the lower the temperature, the faster the recovery was. The recovery times were 76 s, 94 s and 115 s at 400, 450 and 500 °C, respectively. In general, the response times were lower than 80 s and the recovery times were lower than 115 s at the three temperatures evaluated.

3.2.3. Accuracy and precision

In a new experiment, samples of 0.200 mbar of H_2 in Ar were measured in triplicate. It's important to note that this H_2 partial pressure wasn't included in the calibration curve. This choice was made to measure the accuracy and precision in the lower region of linearity (0.020 – 1.000 mbar). Accuracy was determined as the percentage recovery between the measured partial pressure, which is calculated using the calibration curve, and the nominal value. Precision was calculated as the coefficient of variation (CV) of the replicates, as detailed in Table 2.

In Table 2, sensor measurements closely approximated nominal partial pressure, as indicated by the recoveries, which fell within the acceptable range defined by the Association of Official Analytical Chemists (AOAC, 95 % – 105 % [24]). Precision exhibited consistent behavior across all three temperatures, with CV ranging from 0.8 % to 1.1 %. Comparing these values to the accepted criteria (<4%) [25], it

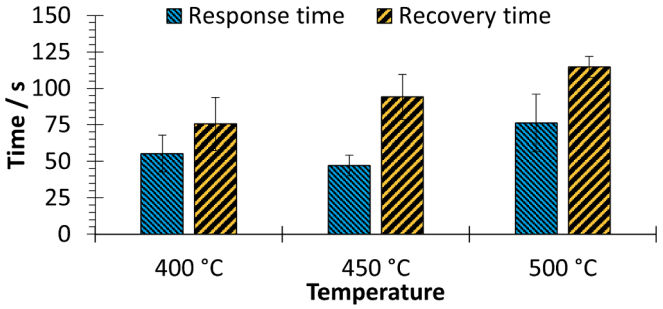

Fig. 8. Response and recovery times obtained at the temperatures evaluated in potentiometric mode.

Table 2
Accuracy and precision data in potentiometric configuration.

Temperature/°C	Measured H_2/mbar	Accuracy(Rec/%)	Precision (CV/%)
400	0.207	103.4	1.1
450	0.208	103.9	0.8
500	0.192	96.0	1.1

Table 1
Calibration curves data of the sensors and Nernst equation values.

T /°C	Slope			Y–intercept			R^2
	Exp. /mV	Nernst /mV	Error/%	Exp. /mV	Nernst /mV	Error /%	
400	–28.15	–29.00	–2.9	–188.18	–200.34	–6.1	0.9982
450	–30.31	–31.17	–2.7	–204.34	–215.30	–5.1	0.9965
500	–32.02	–33.31	–3.9	–225.96	–230.10	–1.8	0.9964

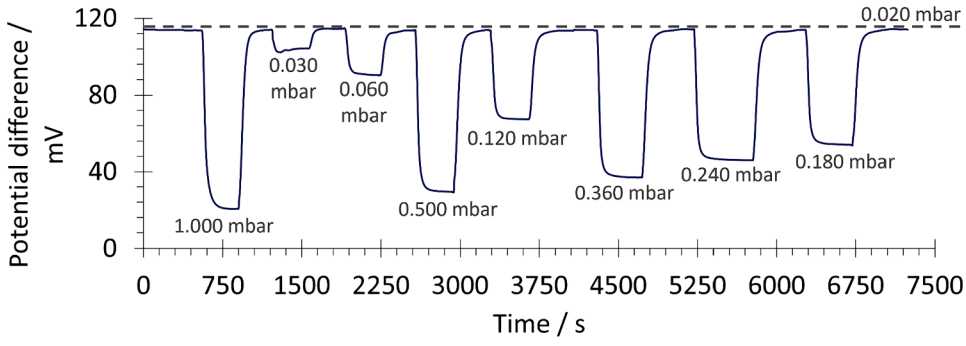

Fig.7. DRR curve obtained at 400 °C in potentiometric mode.

demonstrates the sensors' high measurement precision. Then, the sensors reliably provide accurate measurements within the tested linear range.

3.3. Amperometric mode

3.3.1. Applied voltage determination

First, the applied voltage between electrodes was determined. For that, a concentration in the WE of 0.040 mbar was fixed and the intensity was measured when 50 mV, 150 mV, 250 mV and 500 mV were applied between electrodes. The results are shown in Table 3.

As can be observed in Table 3, the current registered at 50 mV (151 μA) was significantly low compared with the intensities registered at higher voltages. At 150 mV, the maximum current flowed between the WE and the CE (700 μA). Similar current was obtained at 250 mV (690 μA). When 500 mV were applied, the current decreased significantly to 510 μA.

The increase in current from 50 to 150 mV can be attributed to the rise in the applied voltage, indicating a charge transfer potential region within this voltage range. Note that, at applied potentials higher than 150 mV, small variations of the measured current were observed suggesting a diffusion-controlled potential region [10,26]. Therefore, the voltage that was decided to be applied between electrodes was 150 mV.

3.3.2. Sensor's calibration

Then, calibration curves were obtained with the sensors by applying 150 mV between WE and CE. Sensors were evaluated between pure Ar and 0.034 mbar H_2. For instance, Fig. 9 shows the measured current vs. time at 400 °C.

Fig. 9 shows that, when 0.010 mbar of H_2 were injected in the WE, a very small increment in the current was detected by the sensor (0.3 μA of increment). In contrast, from 0.020 to 0.028 mbar, the steps were significantly higher (10 μA of increment after each step). Finally, from 0.028 mbar to 0.034 mbar, the intensity increment was slightly lower (3 to 5 μA of increase).

To deeply evaluate the sensors, calibration curves were obtained by plotting the corrected intensity vs. P_{H2} at each temperature (see Fig. 10). The corrected intensity was obtained by subtracting the argon signal to all the measurements. Error bars represents the standard deviation between three different sensors.

In Fig. 10 is depicted that a linear trend was obtained at the three temperatures evaluated. At 400 °C (Fig. 10-A), linear range was determined between 0.020 mbar and 0.030 mbar. In contrast, at 450 °C the linearity was observed between 0.012 mbar and 0.024 mbar. At 500 °C, a similar behavior was observed, with a linear range between 0.010 and 0.022 mbar. The linear range was displaced to lower values when the temperature increased. This was attributed to the rise in conductivity with the temperature [27,28]. In addition, note that the error bars in Fig. 10 showed good reproducibility between sensors. The calibration curves and the limit of detection (LOD) [22] obtained at each temperature are shown in Table 4.

As can be observed in Table 4, at 400 °C, the slope i.e., the sensitivity of the sensors, was $3.4{\cdot}10^3$ μA·mbar^{-1} between 0.020 and 0.030 mbar. In contrast, at 450 °C, sensitivity was 20 times higher than at 400 °C ($6.6{\cdot}10^4$ μA·mbar^{-1}), with a lower limit of detection (0.002 mbar) and a linearity in lower hydrogen partial pressures (0.012 – 0.024). At 500 °C, a slightly lower sensitivity was observed ($4.7{\cdot}10^4$ μA·mbar^{-1}) with also a slightly displaced linear range to lower hydrogen partial pressures (0.010 – 0.022 mbar). The increase of sensitivity observed from 400 °C to 450 °C – 500 °C was also attributed to the increase in proton conductivity with the temperature [27,28].

Table 3
Current vs applied voltage at 500 °C with 0.040 mbar H_2 in the WE.

Applied voltage / mV	Current / μA
50	151
150	700
250	690
500	510

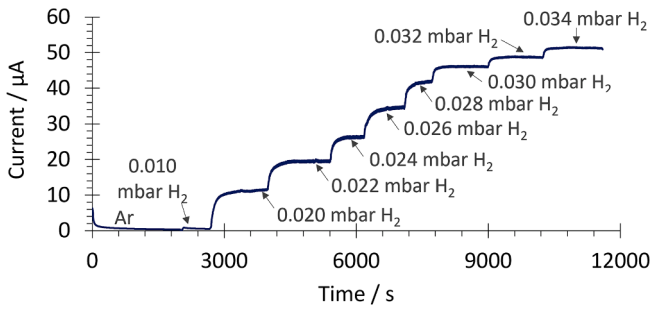

Fig. 9. Measured current vs. time when 150 mV were applied between electrodes at 400 °C.

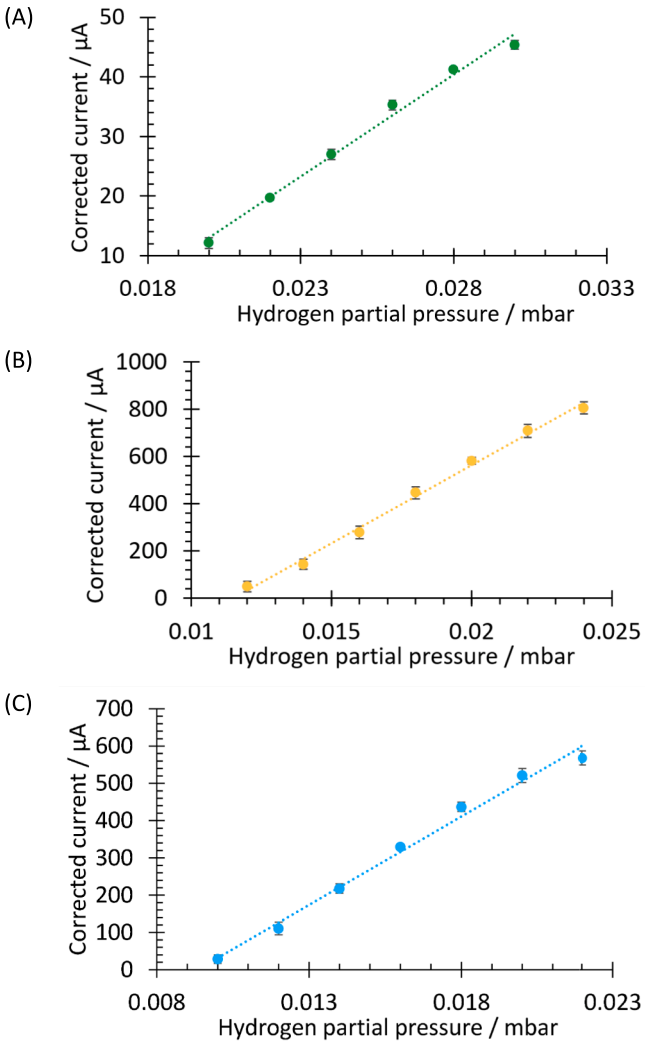

Fig. 10. Calibration curves obtained in amperometric configuration at (A) 400 °C, (B) 450 °C and (C) 500 °C.

3.3.3. DRR curve

Similar to the measurement performed in potentiometric mode, a DRR curve was performed with the sensors in amperometric configuration. Initially, argon was introduced into the working electrode (WE),

Table 4
Calibration curves obtained in amperometric mode and LOD.

T / °C	Calibration curves	R^2	Linearity /mbar	LOD /mbar
400	$(I/\mu A) = 3.4 \cdot 10^3 \cdot (P_{H2}/mbar) - 55$	0.9982	0.020—0.030	0.004
450	$(I/\mu A) = 6.6 \cdot 10^4 \cdot (P_{H2}/mbar) - 758$	0.9965	0.012—0.024	0.002
500	$(I/\mu A) = 4.7 \cdot 10^4 \cdot (P_{H2}/mbar) - 443$	0.9964	0.010—0.022	0.002

which served as the recovery concentration. The hydrogen partial pressures were randomly changed between 0.020 and 0.030 mbar at 400 °C, and from 0.010 to 0.022 mbar at 450 °C and 500 °C. Once the response had stabilized, a pure argon flow was reintroduced in the WE (Fig. 11).

Fig. 11 indicates that a rapid rise in the intensity was observed with each hydrogen partial pressure step. Furthermore, it is observed that signal consistently returned to recovery signal after each decrease in hydrogen concentration. Therefore, in Fig. 12 were plotted the response and recovery times at each working temperature. Error bars were calculated by considering three different sensors and all the measurements performed at different concentrations of H_2.

The fastest response time was achieved at 450 °C (176 s), as shown in Fig. 12. At 400 °C and 500 °C, the response times were higher: 265 s and 358 s, respectively. Recovery times were very similar at the three temperatures (25 – 39 s).

3.3.4. Accuracy and precision

Finally, the accuracy and precision of the sensors were evaluated in a new series of experiments. The same procedure used in potentiometric mode was followed. In this case, samples of 0.025 mbar H_2 were tested at 400 °C while samples of 0.015 mbar H_2 were tested at 450 °C and 500 °C. These specific partial pressures were selected to ensure they fell within the range covered by the calibration curve obtained at each respective temperature. These parameters are described in Table 5.

Table 5 displays the measured values obtained by the sensors when exposed to each H_2 sample, specifically 0.025 mbar at 400 °C and 0.015 mbar at 450 °C and 500 °C. The measured values aligned with the nominal partial pressure, as indicated by the recoveries. The recoveries ranged between 97.7 % and 104.5 %, falling within the accepted range criteria set by the AOAC (95 – 105 % [24]). In terms of precision, similar behaviour was observed at all three temperatures, with coefficients of variation ranging between 0.5 % and 1.4 %. When comparing these values with the accepted criteria of < 4 % [25], high measurement precision is obtained. Thus, it can be concluded that the sensors can provide reliable measurements in the range evaluated.

Overall, the sensors exhibited exceptional sensitivity, accuracy, and precision in both modes. Regarding response and recovery times, they also offered, fast and equilibrated response and recovery times in potentiometric mode and a very fast recovery time in amperometric mode. Finally, the complementary linear ranges of operation between both modes expanded the sensors' operational capabilities, making them highly versatile and adaptable to various scenarios.

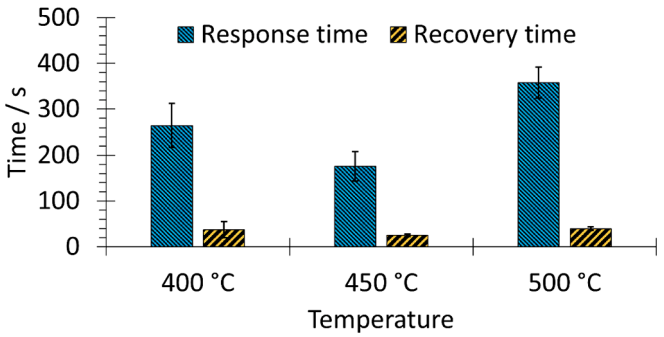

Fig. 12. Response and recovery times in amperometric configuration at 400 °C, 450 °C and 500 °C.

Table 5
Accuracy and precision data obtained in amperometric mode.

T /°C	Nominal P_{H2} / mbar	Measured P_{H2} / mbar	Accuracy(Rec / %)	Precision (CV / %)
400	0.025	0.024	97.7	0.5
450	0.015	0.016	104.5	0.7
500	0.015	0.015	100.5	1.4

4. Conclusions

$BaCe_{0.6}Zr_{0.3}Y_{0.1}O_{3-\alpha}$ was effectively shaped into closed tubes using stereolithography, exhibiting high layer adhesion and densification (97.9 %). The XRD analysis confirmed the presence of BCZY cubic phase with impurities of $Ba_5(OH)(PO_4)_3$. This undesirable phase had a minor impact on sensor' performance.

In potentiometric mode, the sensors displayed Nernstian behavior across evaluated temperatures, with low deviations (≤3.9 % in the slope, ≤ 6.1 % in the Y-intercept). Response times were consistently under 90 s, with recovery times below 125 s. Accuracy and precision met AOAC criteria, with recoveries of 96 % – 104 % and coefficients of variation under 1.1 %.

Amperometric mode showed sensitivity variations with temperature, peaking at 450 °C ($6.6 \cdot 10^4$ μA/mbar) and 500 °C ($4.7 \cdot 10^4$ μA/mbar). Linearity shifted with temperature, covering complementary pressure ranges to potentiometric mode. Response times were under 358 s, with recovery times always below 40 s. Accuracy and precision also met AOAC criteria, with recoveries of 98 % – 105 % and coefficients of variation under 1.4 %.

Note that the best sensitivities in amperometric mode were obtained at 450 °C and 500 °C, extending the range of detectable hydrogen partial pressures of potentiometric mode. This versatility positions these sensors as promising tools for various applications, offering real-time, accurate, and precise measurements of low hydrogen partial pressures.

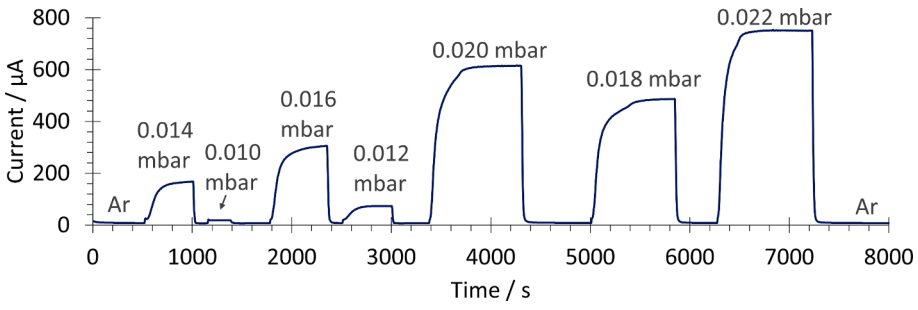

Fig. 11. Dynamic response/recovery curve obtained at 450 °C in amperometric configuration.

CRediT authorship contribution statement

Antonio Hinojo: Data curation, Formal analysis, Investigation, Methodology, Resources, Validation, Writing – original draft, Writing – review & editing. **Enric Lujan:** Data curation, Formal analysis, Investigation, Methodology, Resources, Validation, Writing – original draft, Writing – review & editing. **Jordi Abella:** Conceptualization, Funding acquisition, Investigation, Methodology, Project administration, Supervision, Validation, Writing – review & editing. **Sergi Colominas:** Conceptualization, Funding acquisition, Investigation, Methodology, Project administration, Supervision, Validation, Writing – review & editing.

Declaration of competing interest

The authors declare that they have no known competing financial interests or personal relationships that could have appeared to influence the work reported in this paper.

Data availability

The authors do not have permission to share data.

Acknowledgments

The authors express their gratitude to the Department of Chemical Engineering and Materials Science at IQS-URL (Dr. C. Colominas and Ms. N. Sala) for their contribution to the X-ray diffraction analysis. Enric Lujan acknowledges the financial support provided by the Secretariat of Universities and Research of the Department of Education and Knowledge of the Generalitat de Catalunya (Grant No. 2021 FISDU 00136).

Funding

Project PID2022-140347OB-I00 funded by MCIN/AEI/10.13039/501100011033/ and by ERDF A way of making Europe.

References

[1] C.M. Hussain, R. Keçili, Electrochemical techniques for environmental analysis, in: Modern Environmental Analysis Techniques for Pollutants, Elsevier, 2020: pp. 199–222. doi: 10.1016/B978-0-12-816934-6.00008-4.
[2] N. Holstein, W. Krauss, J. Konys, F.S. Nitti, Development of an electrochemical sensor for hydrogen detection in liquid lithium for IFMIF-DONES, Fusion Eng. Des. 146 (2019) 1441–1445, https://doi.org/10.1016/j.fusengdes.2019.02.100.
[3] N. Holstein, W. Krauss, F.S. Nitti, Electrochemical hydrogen detection in DONES loop materials, Nuclear Materials and Energy 31 (2022) 101192, https://doi.org/10.1016/j.nme.2022.101192.
[4] N. Holstein, W. Krauss, F.S. Nitti, Detection of hydrogen as impurity in liquid lithium: An electrochemical hydrogen-sensor for IFMIF-DONES, Fusion Eng. Des. 178 (2022) 113085, https://doi.org/10.1016/j.fusengdes.2022.113085.
[5] H. Iwahara, Proton conducting ceramics and their applications, Solid State Ion 86–88 (1996) 9–15, https://doi.org/10.1016/0167-2738(96)00087-2.
[6] C.J.T. Grotthuss, Sur la décomposition de l'eau et des corps qu'elle tient en dissolution à l'aide de l'électricité galvanique, Annales De Chimie Et De Physique 58 (1806) 54–73.
[7] T. Norby, Solid-state protonic conductors: principles, properties, progress and prospects, Solid State Ion 125 (1999) 1–11, https://doi.org/10.1016/S0167-2738(99)00152-6.
[8] F. Shimojo, K. Hoshino, H. Okazaki, Effects of doped acceptor ions on proton diffusion in perovskite oxides: a first-principles molecular-dynamics simulation, J. Phys. Condens. Matter 10 (1998) 285–294, https://doi.org/10.1088/0953-8984/10/2/007.
[9] N. Agmon, The Grotthuss mechanism, Chem Phys Lett 244 (1995) 456–462, https://doi.org/10.1016/0009-2614(95)00905-J.
[10] J. Janata, Principles of Chemical Sensors, 2nd ed., Springer US, Boston, MA, 2009. doi: 10.1007/b136378.
[11] A. Marcucci, F. Zurlo, I.N. Sora, E. Placidi, S. Casciardi, S. Licoccia, E. Di Bartolomeo, A redox stable Pd-doped perovskite for SOFC applications, J Mater Chem A Mater 7 (2019) 5344–5352, https://doi.org/10.1039/C8TA10645B.
[12] Y. Zhang, B. Chen, D. Guan, M. Xu, R. Ran, M. Ni, W. Zhou, R. O'Hayre, Z. Shao, Thermal-expansion offset for high-performance fuel cell cathodes, Nature 591 (2021) 246–251, https://doi.org/10.1038/s41586-021-03264-1.
[13] S. Ricote, R.J. Kee, W.G. Coors, Slip Casting and Solid-State Reactive Sintering of BCZY(BaCexZr0.9−xY0.1O3−d)-NiO/BCZY Half-Cells, Membranes (basel) 12 (2022) 242, https://doi.org/10.3390/membranes12020242.
[14] T. Mahata, S.R. Nair, R.K. Lenka, P.K. Sinha, Fabrication of Ni-YSZ anode supported tubular SOFC through iso-pressing and co-firing route, Int J Hydrogen Energy 37 (2012) 3874–3882, https://doi.org/10.1016/j.ijhydene.2011.04.207.
[15] A. Hinojo, E. Lujan, M. Nel-Lo, J. Abella, S. Colominas, Potentiometric Hydrogen Sensor with 3D-Printed BaCe0.6Zr0.3Y0.1O3-α Electrolyte for High-Temperature Applications, Sensors (basel) 22 (2022), https://doi.org/10.3390/s22249707.
[16] A. Hinojo, E. Lujan, M. Nel-lo, S. Colominas, J. Abella, BaCe0.6Zr0.3Y0.1O3-α electrochemical hydrogen sensor for fusion applications, Fusion Engineering and Design 188 (2023) 113452, https://doi.org/10.1016/j.fusengdes.2023.113452.
[17] A. Hinojo, I. Soriano, J. Abellà, S. Colominas, Evaluation of High-Temperature Hydrogen Sensors Based on BaCe0.6Zr0.3Y0.1O3-α and Sr(Ce0.9Zr0.1)0.95Yb0.05O3-α Perovskites for Industrial Applications, Sensors 20 (2020) 7258, https://doi.org/10.3390/s20247258.
[18] S. Ricote, G. Caboche, O. Heintz, Synthesis and proton incorporation in BaCe0.9−x Zr x Y0.1O3−δ, J Appl Electrochem 39 (2009) 553–557, https://doi.org/10.1007/s10800-008-9745-6.
[19] J. Tong, D. Clark, M. Hoban, R. O'Hayre, Cost-effective solid-state reactive sintering method for high conductivity proton conducting yttrium-doped barium zirconium ceramics, Solid State Ion 181 (2010) 496–503, https://doi.org/10.1016/j.ssi.2010.02.008.
[20] F.M.M. Snijkers, A. Buekenhoudt, J. Cooymans, J.J. Luyten, Proton conductivity and phase composition in BaZr0.9Y0.1O3−δ, Scr Mater 50 (2004) 655–659, https://doi.org/10.1016/j.scriptamat.2003.11.028.
[21] AOAC, Official Methods of Analysis of AOAC INTERNATIONAL, 21st ed., 2019.
[22] J.N. Miller, J.C. Miller, R.D. Miller, Statistics and Chemometrics for Analytical Chemistry, Seventh Edition, Pearson Educational Limited, Harlow, UK, 2018.
[23] C. Maccà, Response time of ion-selective electrodes, Anal Chim Acta 512 (2004) 183–190, https://doi.org/10.1016/j.aca.2004.03.010.
[24] AOAC, Standard Format and Guidance for AOAC Standard Method Performance Requirement (SMPR) Documents, (2011) 1–27.
[25] AOAC, Definitions And Calculations Of Horrat Values From Intralaboratory Data., (2004).
[26] J. Zosel, Amperometry, in: Encyclopedia of Applied Electrochemistry, Springer New York, New York, NY, 2014: pp. 65–73. doi: 10.1007/978-1-4419-6996-5_216.
[27] N. Bonanos, Ionic conductivity of gadolinium-doped barium cerate perovskites, Solid State Ion 35 (1989) 179–188, https://doi.org/10.1016/0167-2738(89)90028-3.
[28] S. Barison, M. Battagliarin, T. Cavallin, L. Doubova, M. Fabrizio, C. Mortalò, S. Boldrini, L. Malavasi, R. Gerbasi, High conductivity and chemical stability of BaCe1−x−yZrxYyO3−δ proton conductors prepared by a sol–gel method, J Mater Chem 18 (2008) 5120, https://doi.org/10.1039/b808344d.